In-situ monitoring of corrosion mechanisms and phosphate inhibitor surface deposition during corrosion of Zinc Magnesium Aluminium (ZMA) alloys using novel time-lapse microscopy.

James Sullivan[a], Nathan Cooze[a], Callum Gallagher[a], Tom Lewis[a], Tomas Prosek[b], Dominique Thierry[b]
[a] College of Engineering, Swansea University, Singleton Park, Swansea SA2 8PP
[b] Instituit de la corrosion, 220 Rue Pierre Rivoalon, 29200 Brest, France

Abstract
In-situ time-lapse optical microscopy was used to examine the microstructural corrosion mechanisms in three zinc-magnesium-aluminium (ZMA) alloy coated steels immersed in 1% NaCl pH 7. Preferential corrosion of $MgZn_2$ lamellae within the eutectic phases was observed in all the ZMA alloys followed by subsequent dissolution of Zn rich phases. The total extent and rate of corrosion, measured using time-lapse image analysis and scanning vibrating electrode technique **(**SVET) estimated mass loss, decreased as Mg and Al alloying additions were increased up to a level of 3 wt% Mg and 3.7 wt% Al. This was probably due to the increased presence of MgO and Al_2O_3 at the alloy surface retarding the kinetics of cathodic oxygen reduction. The addition of 1 x 10^{-2} mol/dm^3 Na_3PO_4 to 1% NaCl pH 7 had a dramatic influence on the corrosion mechanism for a ZMA with passivation of anodic sites through phosphate precipitation observed using time-lapse. Intriguing rapid precipitation of filamentous phosphate was also observed and it is postulated that these filaments nucleate and grow due to super saturation effects. Polarisation experiments showed that the addition of 1 x 10^{-2} mol/dm^3 Na_3PO_4 to the 1% NaCl electrolyte promoted an anodic shift of 50mV in open circuit potential for the ZMA alloy with a reduction in anodic current of 2.5 orders of magnitude suggesting that it was acting primarily as an anodic inhibitor supporting the inferences from the time-lapse investigations. These phosphate additions resulted in a 98% reduction in estimated mass loss as measured by SVET demonstrating the effectiveness of phosphate inhibitors for this alloy system.

1. Introduction
There is significant interest in steel companies world wide in the production of ternary zinc-magnesium-aluminium (ZMA) galvanised alloy coatings for the cathodic protection of steel substrates. This new class of coating offer potential improvements in corrosion resistance that are of interest to a wide variety of markets from construction to automotive. This increase in corrosion resistance offers improved coating lifetimes for lower coating weights providing a significant cost benefit to the manufacturer. The development of ZMAs follows enhancements to the corrosion resistance of hot dipped galvanised steel coatings over the last 20 years through binary alloy additions such as Al. Al additions of 5 wt% (Galfan) and 55 wt% (Galvalume) have demonstrated significant advances in corrosion resistance over traditional Hot Dipped Galvanised (HDG) coatings [1,2]. The morphology of the microstructure and production conditions of these binary alloys have dramatic effects on the corrosion resistance of Zn/Al alloy coated steels with the corrosion rate related to dendrite size, nucleation rate and volume fraction of phases [3,4,5]. Attempts have been made to further improvement Zn/Al alloy coatings on steel through small ternary additions of Mg of 0.05 wt% but resulted in negative effects on the cut edge corrosion resistance due to microstructural changes [6]. Current research in this field has focussed on higher additions of ternary Mg of up to 3 wt % and these alloys have demonstrated increased corrosion protection over standard Zn - 0.2 wt% Al galvanised coatings in accelerated corrosion tests [7,8,9,10]. The mechanism of the increased corrosion resistance of these alloys, especially in chloride rich environments, has been investigated by a number of authors with regards to stable corrosion product film formation [7,11,12,13,14,15] and the effect of Carbon Dioxide in the atmosphere [16]. The increased resistance of such coatings

to organic coating delamination has also been investigated by focussing on the electrochemical behaviour of $MgZn_2$ and Zn phases that are prevalent in ZMA alloys [17]. The introduction of Mg into these alloys can produce a variety of phases within the microstructure [18,19] and thus exploration of the effect of these phases on the corrosion performance is critical in choosing the best alloy compositions for production. In situ aqueous time-lapse microscopy has been previously demonstrated by the authors to show that $MgZn_2$ phases were preferentially attacked in the aqueous corrosion of a ZMA containing 1.5-2 wt% Mg 1.5-2 wt% Al additions [20]. The initial stages of corrosion and preferential phase attack of such alloys has also been assessed at a nanoscopic level in other research [21].

The development of new ZMA alloy coatings is concurrent with the drive to find replacements for chromate corrosion inhibitors that are being phased out of use through REACH legislation by 2017. Thus, an understanding of the behaviour of these new alloys with chromate replacement technologies is of significant interest within a number of industrial sectors. Phosphate ions have been shown to work effectively as a corrosion inhibitor on galvanised steels in a number of investigations [22,23,24,25] but there is currently little research on the evaluation of such ions on ZMA alloy coatings.

This current paper demonstrates a novel time-lapse microscopy technique that enables in situ monitoring of the microstructural aqueous corrosion mechanisms of three ZMA alloys with increasing Mg and Al alloy additions. The technique provides valuable mechanistic and rate information regarding preferential phase attack within the microstructure of the alloys allowing the assessment of these alloy additions on the corrosion of the alloys to be determined. The Scanning vibrating electrode technique (SVET) was used to evaluate metal loss over a 24 hour period to provide an additional assessment of the performance of the three ZMAs. In addition, a further investigation involving the novel time lapse technique, SVET and polarisation studies was carried out using one ZMA to assess the mechanism of corrosion inhibition by sodium phosphate.

2. Experimental procedure

2.1 ZMA alloys

The ZMA alloys used in this study had increasing levels of Mg and Al levels. The compositions and coatings thickness of the three alloys are given in Table 1. All alloys were produced under production line conditions from commercial producers.

Table 1. Compositions in weight % (wt %) of the three Zn-Mg-Al (ZMA) alloys under investigation.

Sample	Zn (wt %)	Mg (wt %)	Al (wt %)	Coating thickness (μm)
ZMA 1	98	1	1	10
ZMA 2	96	2	2	10
ZMA 3	93.3	3	3.7	10

2.2 In situ time-lapse optical microscopy for assessment of microstructural corrosion mechanisms of ZMA alloys

A novel system has been developed that allows imaging of corroding surfaces under immersion conditions to be imaged at a microstructural level. The technique has been iterated based on previous research [20] and encompasses a waterproof shroud made of polyethylene that is placed over the lens of a Meiji MT8000 microscope. The base of the shroud encases a glass window that permits imaging of the sample surface whilst the lens is immersed in the electrolyte. A schematic of the microscope set up is given in figure 1.

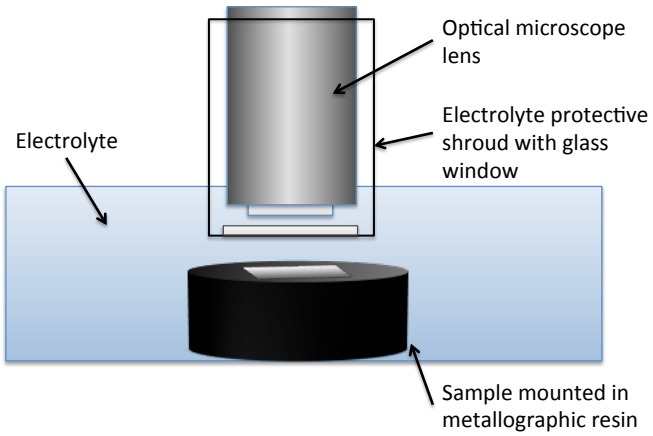

Figure 1. Schematic diagram of in-situ optical microscopy configuration that allows imaging of corroding metals under immersion conditions. The microscope lens is shrouded from the electrolyte by a protective cover containing a glass window to allow imaging of corrosion mechanism within the microstructure of the sample.

Samples of ZMA alloys were prepared by mounting a 20 mm x 20 mm piece of alloy coated steel in phenolic resin and polishing the surface down 2 µm to reveal a flat surface and to remove manufacturing oils and oxides from the surface. The surface was etched using 2% Nital solution to reveal the microstructure, taped with PTFE leaving only a circular feature of diameter 1 mm (area of 0.785 mm^2) exposed. The sample was then securely fixed to a stage in a glass tank using PTFE tape and 250 ml of 1% NaCl pH7 electrolyte added to the tank so that the sample was immersed. The lens of the microscope was then manoeuvred into place so that imaging of the microstructure under the electrolyte could be achieved. Images were captured every two minutes using the time-lapse function of an Infinity 2 digital camera attached to the microscope. The duration of experiments were 17 hours for time-lapse analysis of the three ZMA alloys. Time-lapse videos were compiled from the still images after each experiment using Microsoft Movie Maker.

2.3 In situ time-lapse optical microscopy for assessment of the mechanism of phosphate corrosion inhibition of ZMA alloys

The same experimental setup was used as in section 2.2. For these tests ZMA 2 was used as the base substrate and experiments were initiated in 1% NaCl to establish initial corrosion activity. After 3 hours additions of Na_3PO_4 were made to the electrolyte to establish a concentration of 1 x 10^{-2} mol/dm^3 Na_3PO_4 and time-lapse images taken over a total of 36 hours to assess effect of phosphate on the corrosion mechanisms.

2.4 Scanning vibrating electrode technique (SVET) for the assessment of corrosion performance of ZMA alloys and the effectiveness of phosphate inhibition on ZMA systems

SVET scans were performed on the three ZMA alloys to provide an additional insight into their relative corrosion performance. ZMA samples were prepared as in the same manner for time-lapse experiments as described in section 2.2 but an area of 100 mm^2 was left exposed on the sample surface. The SVET probe made 50 measurements along the length of the sample and 50 measurements across the samples width generating a matrix of 2500 data points for each scan. The SVET tests were carried out in 1% NaCl pH 7 solution, one scan was taken every hour for 24 hours and three repeat tests for each material were carried out. The dissolved oxygen concentration in

bulk solution was assumed to be constant at 2.8 x 10^{-4} mol dm^{-3}, the equilibrium concentration for air saturated water, and all tests were carried out at 25°C. For the assessment of phosphate inhibition samples of a single alloy coated steel, ZMA 2, were prepared in the same manner and then tested in 1% NaCl containing a) no inhibitor b) 1 x 10^{-4} mol/dm^3 Na_3PO_4 c) 1 x 10^{-2} mol/dm^3 Na_3PO_4 for 24 hours.

2.4.1 SVET apparatus and calibration

The SVET has proved to be valuable tool in the investigation of cut edge corrosion in zinc coated and organically coated steels. [3,4,5,6,23,26,27,28,29,]. The SVET apparatus is fully described elsewhere [30,31,32]. The SVET consists of a glass encased, 125 μm diameter Platinum wire micro-tip that is vibrated at a constant frequency, amplitude and height above a corroding surface submerged in electrolyte. The SVET detects an alternating potential at the vibration frequency that is proportional to the potential gradient in solution in the direction of vibration. Movement of the microtip is stepwise and controlled by a micro manipulator stage (Time and Precision) in three dimensions with PC control and a lockin amplifier (EG & G model 7625) serves to control the frequency of vibration and also measure the signal detected by the probe. Vibration is provided from the lockin amplifier via an amplifier at a frequency of 140 Hz with the drive voltage producing an amplitude of probe vibration of 25 μm.

The SVET was used to show the location and intensity of anodes and cathodes on corroding surfaces. The SVET probe was scanned over the surface of a sample in the x, y and z directions at a fixed height of 100 μm. At a site of corrosion potential fields are set-up in solution by ionic current flux passing through the electrolyte emanating from the anodic site. The SVET probe cuts through these lines and registers an alternating potential that is proportional to the potential gradient in the direction of vibration. The SVET signal is thus directly proportional to the component of ionic current density in direction of vibration at the scan height.

Calibration of the SVET was achieved using a two compartment cell. Each compartment contains a Pt electrode and the electrolyte under investigation and the compartments are linked by a vertically oriented glass tube of 4.8 mm internal diameter. Calibration was achieved by placing the SVET tip inside the vertical bore of the glass tube. Different currents were passed through this glass tube using a nano-galvanostat and the current density calculated for the area of the glass tube (radius = 2.4 x 10^{-3} m). The tube allows the lines of current flux to align vertically along its length and thus the SVET tip is vibrated in an area of uniform current density. For each current density the SVET voltage was measured and was found to vary linearly with applied current density. The gradient of a plot of current density versus SVET voltage provides a calibration factor for the instrument and a typical calibration factor in 1% NaCl was 90,000 Am^{-2} V^{-1}. The use of this tube cell for calibration is rapid and independent of probe height and provides a rapid means of converting voltage data detected from the SVET into Am^{-2}.

2.4.2 Manipulation of SVET data

Data from the SVET can be used to semi-quantitatively estimate metal loss over time by integration of positive current data and the application of Faraday's law and thus can be used to compare the performance of similar materials. The mass loss data is semi-quantitative due to a number of assumptions made in the calculations and thus the metal loss data should not be used as a direct measure of the samples weight loss. It is very useful however in comparing the performance similar materials such as galvanised steel materials with different coatings or processing conditions. By assuming the corrosion activity occurring on the sample remains constant in the interval between scans and that the corrosion generally involves the release of a particular metal ion, e.g. Zn^{2+}, it is

possible to deliver a value of total metal loss for the 24-hour experiment. This is achieved by integrating the area under the current density as measured by the SVET to obtain a total current for each scan. These currents are converted to total charge per scan using the time interval between scans with Faraday's law then applied to calculate a mass loss of the ion of interest e.g. Zn. A summation of these values for all 24 scans per sample then provides a total mass loss. The mathematical procedure for these calculation is fully described elsewhere [4].

2.4.3 Limitations of SVET technique

There are a number of limitations associated with the assessment of metal loss from the SVET and thus it should be considered as a semi-quantitative technique. The SVET detects only normal component of current flux that emanates from an anode and also any current loops that terminate under the plane of scan of 100 µm will not be detected. The SVET resolution is approximately equal to 1.5 times scan height of 100 µm so it will not detect anodes and cathodes separated by less than this distance. The SVET measures a snapshot of the corrosion for each hour and assumes a constant corrosion rate over that hour whereas in reality this rate could vary. Despite these limitations the SVET has proved to a reliable predictor of corrosion behaviour for Zn coated steel [3,5] and also has compared favourably when compared with external weathering Zn runoff tests [33].

2.5 Polarisation testing of a ZMA alloy in 1% NaCl with additions of Na_3PO_4

Polarisation tests were carried out on samples of alloy ZMA 2 in 1% NaCl containing a) no inhibitor b) 1×10^{-4} mol/dm^3 Na_3PO_4 c) 1×10^{-2} mol/dm^3 Na_3PO_4. The potential was swept from -1.15V to -0.8V at a rate of 0.1mV/s using a Solartron potentiostat. All potentials were measured versus a standard calomel electrode (SCE).

3. Results and discussion

3.1 Examination of the microstructures of the ZMA alloys

Optical microscope images of the microstructures of the three ZMA alloys are shown in figure 2 A-C.

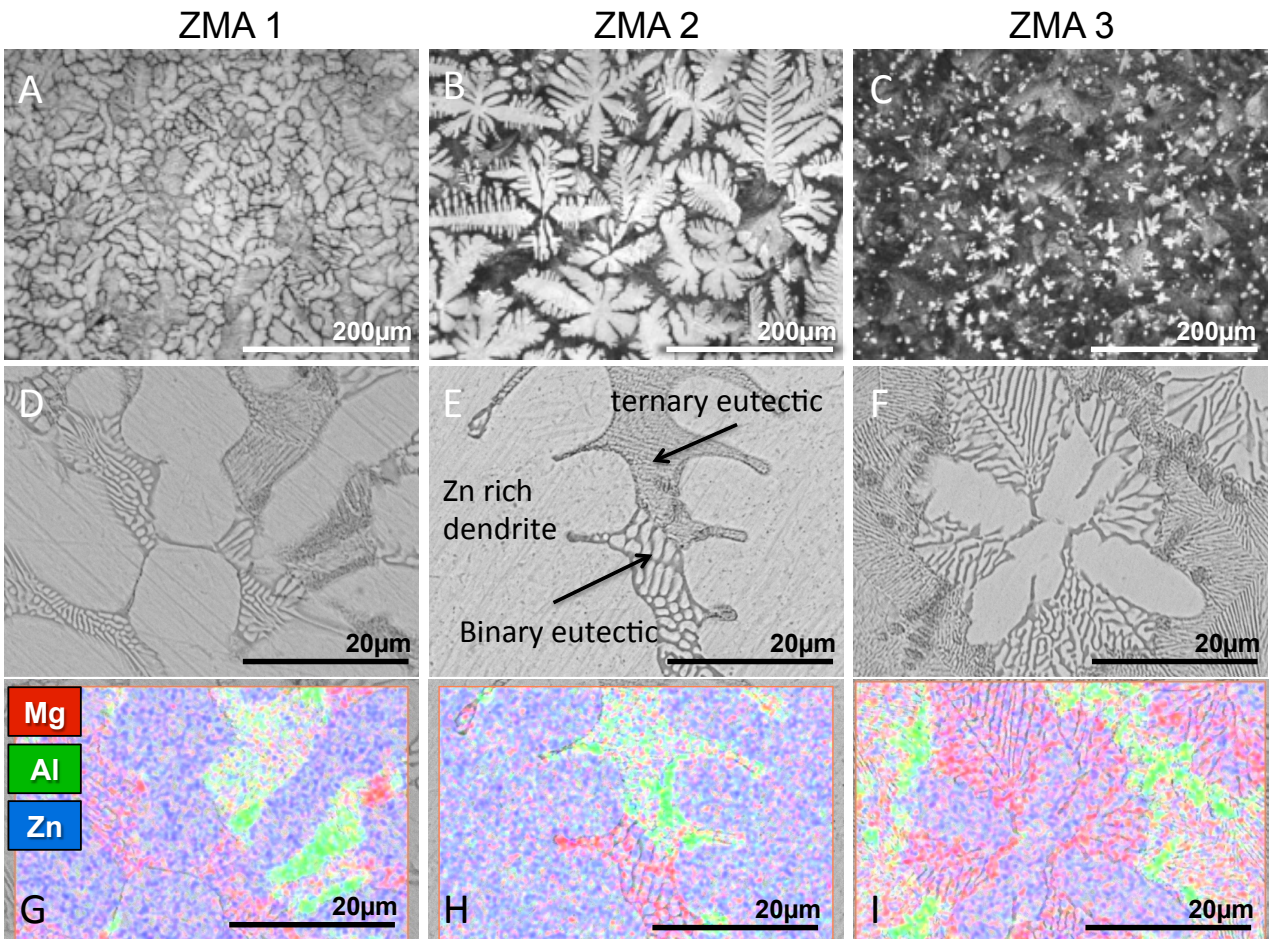

Figure 2. A – C Optical microscope images of the three ZMA samples with increasing alloy contents showing a Zn primary dendritic phase in a matrix of eutectic. An increase in eutectic volume fraction for increasing alloy levels was observed. D – E SEM images of the samples showing coarse binary and fine ternary eutectic phases. G – I EDX analysis of the distribution of Zn, Mg and Al showing that the fine structure eutectic is of ternary composition.

The microstructures were generally composed of primary Zn dendrites and two eutectic phases. The volume fraction of primary Zn rich phase and eutectics varied substantially as alloying additions were increased as shown in figure 3.

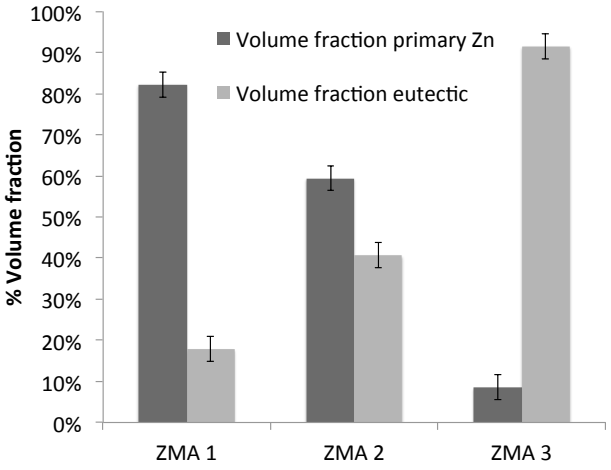

Figure 3. Volume fraction of primary Zn dendrites and eutectic phases for ZMA alloys with increasing Mg and Al levels showing a large rise in eutectic phase fraction as Mg and Al levels are increased to 3 wt% and 3.7 wt% respectively in ZMA 3.

There was a decrease in primary Zn phase volume from 82% in the 1 wt% Mg 1 wt% Al to 9% in the 3 wt% Mg 3.7 wt% Al with a subsequent increase in eutectic phase from 18 to 91% respectively. Furthermore, the morphology of the microstructure varied from sample to sample with coarse primary Zn rich dendrites observed in the 1% and 2% alloyed samples compared with much finer dendrites in the 3% sample potentially indicative of a faster cooling rate for this sample during production. SEM images of the three alloys are shown in figure 2D-F and show the presence of two eutectic phases in the structure, one having coarse lamellae and the other, fine lamellae. EDX analysis of the microstructures is shown in figure 2G-I and demonstrates that the coarse eutectic was composed of Zn and Mg and thus a binary eutectic whereas the finer eutectic was composed of Zn, Mg and Al. Previous research describing the solidification sequence of such alloys has shown that the binary eutectic was composed of Zn and $MgZn_2$ lamellae and the ternary eutectic of Zn, $MgZn_2$ and Al nodules for samples produced under production line conditions [18,20]. In addition, the higher magnification SEM images identified small regions of Al rich dendrites that become more prevalent in the higher alloyed samples and this has been previously identified as a face centred cubic Zn/Al dendritic phase [18].

3.2 Time-lapse corrosion of the ZMA alloys

Figure 4 Images 1-12 show the microstructure of the three ZMA alloys taken at 2 hourly intervals during in-situ immersion in 1% NaCl. From figure 4 images 1-4 it can be seen that a corrosion feature developed within the microstructure of ZMA 1 and grew in size with time towards the centre of the exposed sample area.

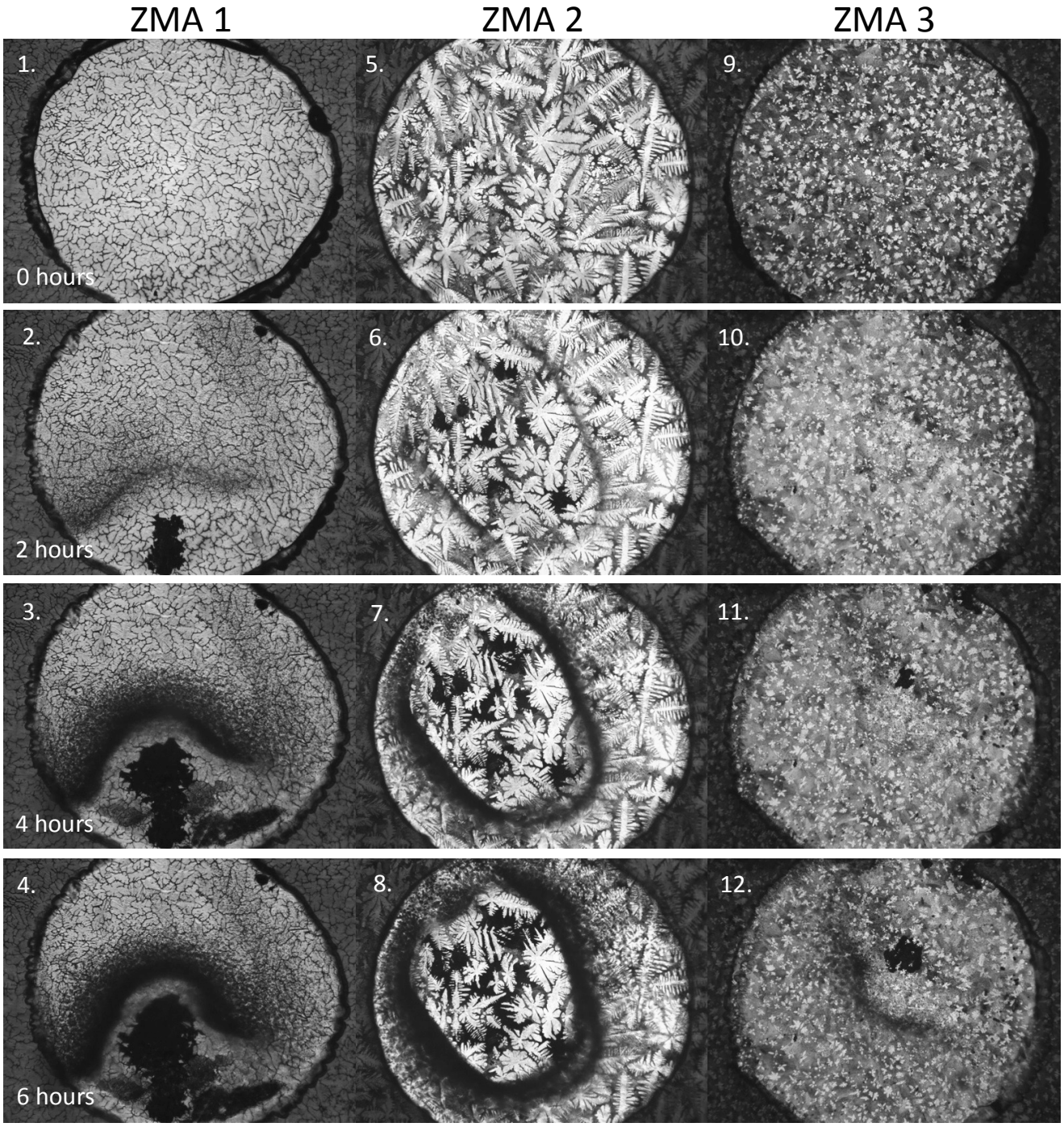

Figure 4. Optical microscope images of ZMA taken in-situ under immersion conditions in 1% NaCl. The Images shown were taken at **two hour** intervals for each alloy. Images 1 – 4 are of alloy ZMA 1 showing the development and progression of a corroding area and a mobile corrosion product ring. Images 5 – 8 are of ZMA 2 showing clear preferential attack of the eutectic phases and the formation of a corrosion product ring between the anodic and cathodic areas on the sample surface. Images 9-12 are of ZMA 3 and show no corrosion for the first 2 hours followed by preferential attack of the eutectic phases and the formation of a corrosion product ring.

The front of the anodic activity progressed preferentially through the eutectic phases as shown in video 1. As anodic growth proceeded a ring of corrosion product was precipitated ahead of the anode indicating the boundary of ionic counter currents of metal and hydroxide ions from the anodic and cathodic activity. The ring of corrosion product was observed to be mobile as the experiment progressed. As anodic activity progressed towards the centre of the exposed sample area, the corrosion product ring dissolved and re-precipitated at a set distance away from the advancing anodic front. This was indicative of pH changes produced as a result of metal dissolution at the anode potentially causing a local reduction in pH that could cause corrosion products to re-solubilise. Figure 4 images 5 - 9 shows comparative results for for ZMA 2. Here, anodic activity clearly initiated and progressed preferentially through the eutectic phases of the microstructure whilst the Zn rich dendrites remained relatively untouched after 6 hours. Once again a clear corrosion product ring formed around the anodic sites indicating the transition to areas of cathodic activity on the surface of the alloy. This mechanism is shown in video 2. Figure 4 images 9 - 12 shows the same experimental conditions but for ZMA 3. Here, there was little corrosion observed in the first 2 hours. Between 2 and 4 hours (figure 4 images 10 and 11) anodic activity initiated and once again progressed through the eutectic phases of the material preferentially leaving islands of primary Zn rich phase. The growth of anodic activity was markedly reduced in comparison to ZMA 1 and 2. This experiment is shown in video 3.

Further exploration of the corrosion mechanisms was carried out using SEM investigations where a circular area of each sample of 0.785 mm^2 was imaged at 0 hours and after 4 hours of exposure to 1% NaCl. This was performed in order to provide further evidence for the preferential phase attack in the microstructure. The results of the experiment for ZMA 1 are shown in figures 5 A-D.

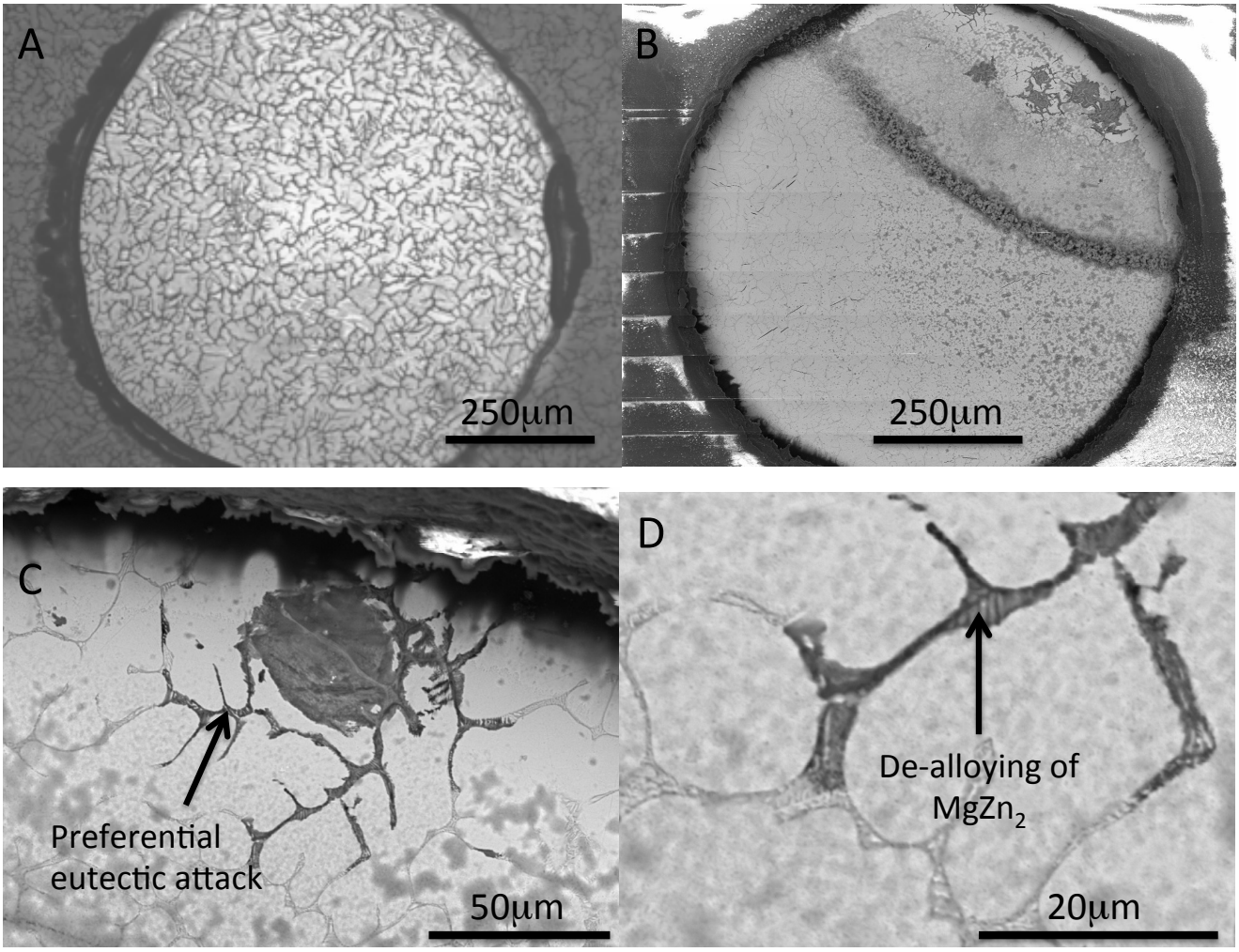

Figure 5 A) Microstructure of ZMA 1 immediately on immersion in 1% NaCl B) The same sampled as in A but imaged after 4 hours in 1% NaCl showing anodic features in the upper right quadrant and a corrosion product ring. C) Magnified anodic region showing preferential corrosion of eutectic phases D) Further examination of preferential corrosion sites showing de-alloying of $MgZn_2$ phase from the eutectic structure.

Figure 5 A shows the microstructure of ZMA 1 on initial exposure to the electrolyte. Figure 5B was taken after 4 hours exposure to 1% NaCl and areas of anodic activity were seen to have initiated in the upper right quadrant of the circular area with a characteristic corrosion product ring forming a boundary between the anodic and cathodic sites. Higher magnification images of an anodic region are given in figure 5 C and D and show that anodic activity was focussed on the eutectic phases between the Zn rich dendrites. The highest magnification image, figure 5 D, demonstrated that regions of binary eutectic had experienced de-alloying of the $MgZn_2$ phase leaving intact regions of Zn lamellar. These images support previous findings that Mg rich phases in ZMA alloys experience preferential attack due to their higher activity and also supports the notion that preferential dissolution in the initial stages of corrosion rapidly develops Mg based corrosion products that provide these alloys with enhanced corrosion resistance compared with standard hot dip Galvanised Zn coatings [15,17,20,21]. As corrosion progressed Zn rich dendrites were indeed corroded from the alloy but the progress of anodic fronts was always associated with eutectic attack in the first instance. The same mechanism was observed in ZMA 2 and 3 with eutectic attack in both samples after 4 hours in 1% NaCl.

From the time-lapse images it was possible to estimate a corroded area per unit time based on the area of anodic attack. This makes an assumption that the majority of the corrosion is progressing laterally across the surface rather than vertically into the specimen. The corrosion was calculated by highlighting the anodic area using Photoshop CS6 on images at hourly intervals from the time-lapse sequences. Photoshop was then used to calculate this area in mm^2 based on a calibration image of a 1 mm standard imaged using identical experimental conditions. Plots of the evolution of corroded area versus time and the total corroded area for ZMA 1, 2 and 3 are shown in figure 6. From figure 6A it can be seen that the growth of corrosion features were relatively linear with time for all the ZMA samples and figure 6B shows that total corroded area reduced as alloying levels increased.

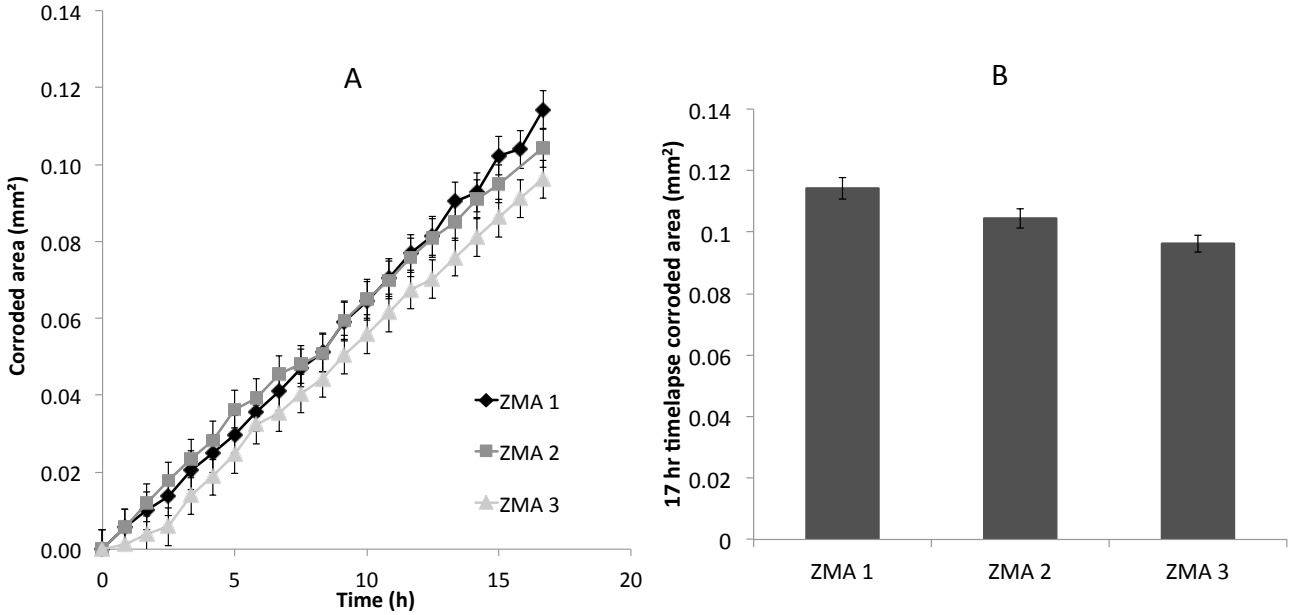

Figure 6 A) Size of corroded area versus time for the three ZMA samples showing a general linear corrosion for each material in 1% NaCl B) Total corroded area after 17 hours in 1% NaCl for each ZMA sample showing reduced corrosion rates with increasing alloy content

Increased alloying additions of Mg and Al changed the phase percentages in the microstructure as shown in figure 3. The total corroded area after 17 hours was plotted versus the volume fraction of eutectic phase in the microstructure and a linear decrease in corroded area was observed as volume fraction of eutectic increased as shown in figure 7.

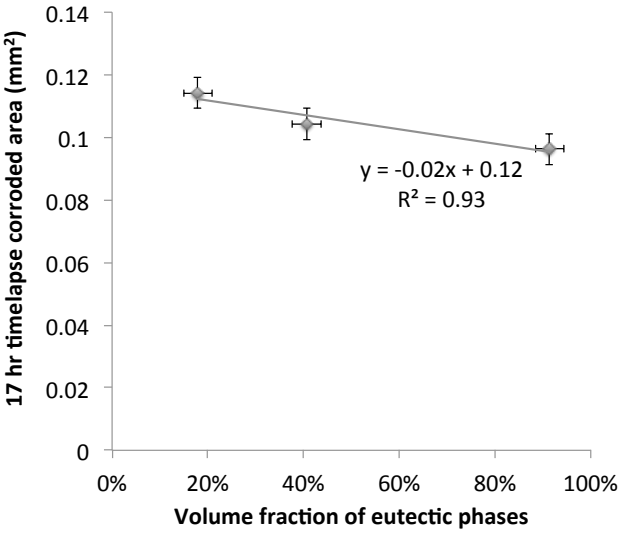

Figure 7. Graph showing the total corroded area of the three ZMA alloys against the percentage of eutectic phases within their structure showing a linear decrease in overall corrosion as the volume fraction of eutectic phases increased.

The quantity of eutectic phase dramatically increases from 18% to 91% from ZMA 1 to ZMA 3. It is maybe counter intuitive that an increased eutectic volume fraction would reduce the corrosion rate given that these phases are preferentially attacked in the microstructure but it would seem that increased levels of Mg and Al in the alloy create more robust oxide layers due to their rapidity of reaction and the passive nature of Al_2O_3 layers. It has been suggested that MgO formation on the surface of such coatings reduces electron transfer rates due to the wide band gap of this oxide [34, 35]. Increasing Al levels within the structure of Zn coatings have been previously shown to reduce the corrosion rate as Al_2O_3 present on the surface of the coatings has a low efficiency for cathodic oxygen reduction [36]. Thus, as alloying levels increase the kinetics of corrosion are reduced but the preferential attack is still thermodynamically more favourable in the $MgZn_2$ regions of the eutectic phases. Visual indicators are provided suggesting this for ZMA 3 in figures 4 images 9 and 10 where anodic activity took a number of hours to initiate in the eutectic regions and a perceptible visual brightening of the surface occurred in the initial hours of exposure to 1% NaCl potentially indicating breakdown of passive oxide layers. This was further highlighted by the slow initial rate of anodic growth over the period of 0-3 hours for ZMA 3 in figure 6 A.

3.3 Scanning vibrating electrode technique (SVET) examination of corrosion behaviour of ZMA alloys

The scanning vibrating electrode technique (SVET) was used to examine the corrosion of the three ZMA alloys over 24 hours in 1% NaCl at pH 7. The SVET was used to estimate the metal loss from the alloys over the 24 hour period as described in section 2.4.2. The metal chosen for use in Faraday's equation was Zn (65.5) as the predominant element in each alloy. It was obviously difficult to predict the contribution to the detected corrosion from each element in the alloy but as the most likely dissolution involved Zn^{2+} and Mg^{2+} ions as demonstrated by the time-lapse investigation, the relative performance relationship between each alloy would be the same if either metal were used in the calculation as each ion has the same charge with a difference arising simply in the ultimate mass loss value. As such the SVET mass estimations have been used in this investigation to simply compare the relative corrosion behaviour of the ZMA alloys rather than provide a precise value for mass lost from each alloy during the experiment.

Mass loss data for the three ZMA alloys as estimated by SVET is presented in figure 8.

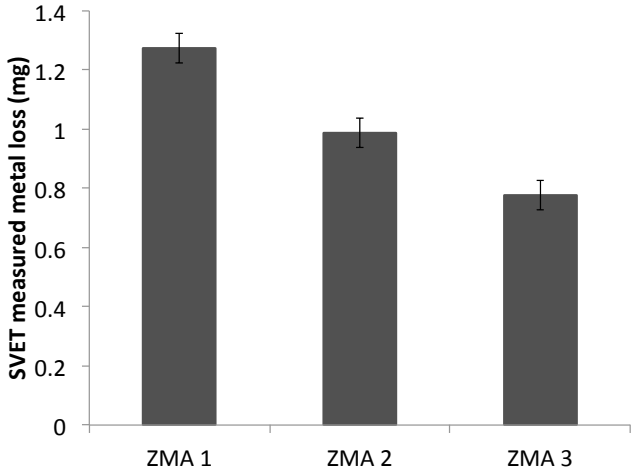

Figure 8. SVET estimated metal loss for the three ZMA alloys after 24 hours exposure in 1% NaCl. A reduction in metal loss was observed for increased levels of Mg and Al alloying additions.

Figure 8 once again demonstrated that increasing alloy additions of Mg and Al in the three ZMA alloys had a beneficial effect in terms of corrosion behaviour. For ZMA 2 the total metal loss was 22% lower than ZMA 1 and for ZMA 3 the metal loss was 39% lower than ZMA 1. These represent a significant performance increase. The performance differences in the SVET investigation were more marked than in the time-lapse experiments and this maybe be due to the limitation of using a 2D area for corrosion measurement in the time-lapse experiments whereas the SVET measurement is dependent on the detection of ionic current flux in the solution above the corroding surface. The SVET measurements were also made over a large area of 100 mm^2 that may have also had an impact in that a number of corrosion features were established over this area over the course of the test thus producing a better average performance indicator for the alloy. Overall though it was encouraging that both experiments provided the same performance ranking for the alloys and in particular provides a degree of confidence in the mass loss predictions from SVET.

3.4 The effect of Sodium Phosphate additions to the corrosion behaviour of a ZMA alloy

Investigations were carried out to assess the behaviour of phosphate ions on the inhibition of corrosion of one of the ZMA alloys, ZMA 2. The mechanism and extent of phosphate action on these alloys is of much interest as phosphate is rapidly becoming the main choice of inhibitor ion in place of chromate in coated steel products due to imminent legislation changes on the use of chromate. The mechanism of phosphate action on ZMA 2 was examined using in situ time-lapse optical microscopy, SVET and polarisation studies through additions of Na_3PO_4 to 1% NaCl pH 7.

3.4.1 Time-lapse investigation of the mechanism of phosphate action on ZMA alloys

Figure 9 images 1-12 shows a 36 hour time-lapse sequence for ZMA 2 immersed in 1% NaCl pH 7 with 1 x 10^{-2} mol/dm^3 Na_3PO_4 added after 3 hours of immersion. Image 1 represents the point of inhibitor addition with subsequent images taken at 3 hour intervals. The sample was left to corrode for 3 hours prior to inhibitor addition in order for some anodic features to become established thus potentially making the mechanism of inhibition easier to observe.

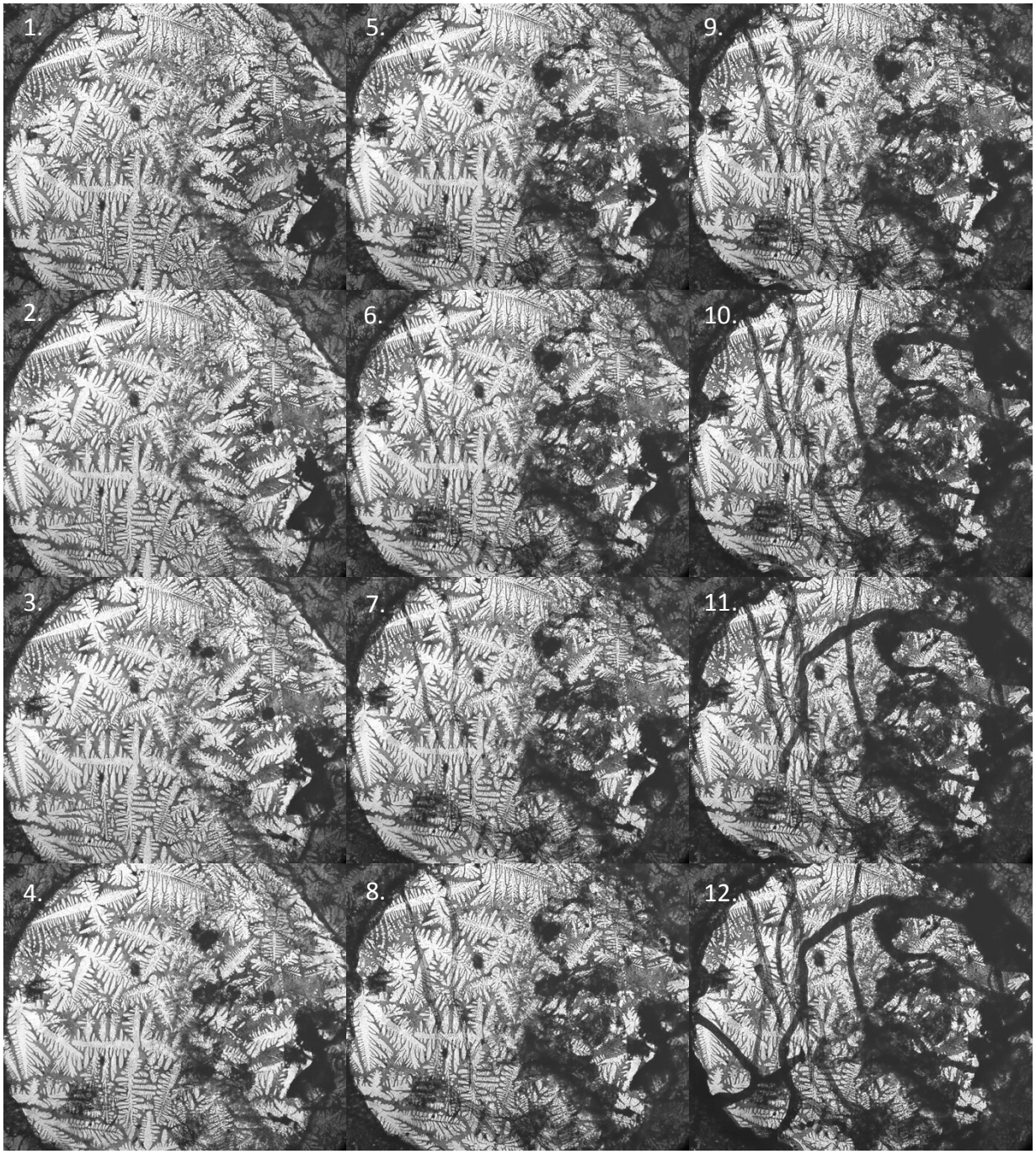

Figure 9. Images 1 – 12. Optical microscope images of ZMA 2 taken in-situ under immersion conditions in 1% NaCl with 1 x 10^{-2} mol/dm^3 Na_3PO_4 additions. The Images shown were taken at **three hour** intervals. Images 1-4 shows the initiation and inhibition of anodic features through precipitation local to the anode. Images 5 – 12 show the development and growth of filamentous precipitates over the surface of the ZMA.

The addition of the phosphate inhibitor dramatically alters the observed corrosion behaviour in comparison to that seen in figure 4 for ZMA 2. The time-lapse sequence can be seen evolving in video 4. After 3 – 6 hours (Figure 9 images 2 and 3) a number of anodic features had initiated over

the sample surface. Growth of these features was restricted however and it was observed that this restricted growth was due to precipitation of a thin solid layer at the anodic site. An image of this deposition at two anodic features is shown in greater detail in figure 10 A. The profile of these precipitates was triangular tapering away from the anodic site suggesting that a local concentration profile of metallic ions had developed from the anode that subsequently reacted with phosphate ions from solution to form a metal phosphate precipitate. The precipitate was very thin given that the underlying microstructure could still be observed through the deposits. As the experiment progressed (figure 9 Images 4 and 5) further anodic features initiated but again their growth was somewhat restricted by phosphate deposition at these sites. After 15 hours (figure 9 image 5) a new morphology of phosphate deposition was observed on the ZMA sample surface. Thin filamentous deposits were seen to rapidly precipitate over large distances on the microstructure. The precipitation initiated from an anodic site but its subsequent growth route was independent of underlying microstructural phases. In fact precipitation was also observed to be independent of the exposed metal on repeated experiments as filaments continued to grow off the metal surface onto the PTFE tape surrounding the exposed area. Initiation and growth of these filamentous deposits continued over the remainder of the 36 hour experiment (figure 9 images 6 – 12) with filaments produced towards the end of the experiment being somewhat thicker in depth as the microstructure could no longer be seen through them.

The precipitation and growth of these filaments was unexpected and of some interest. An image of these filaments in greater detail is show in figure 10 B and SEM/EDX analysis of typical filaments is provided in figure 11.

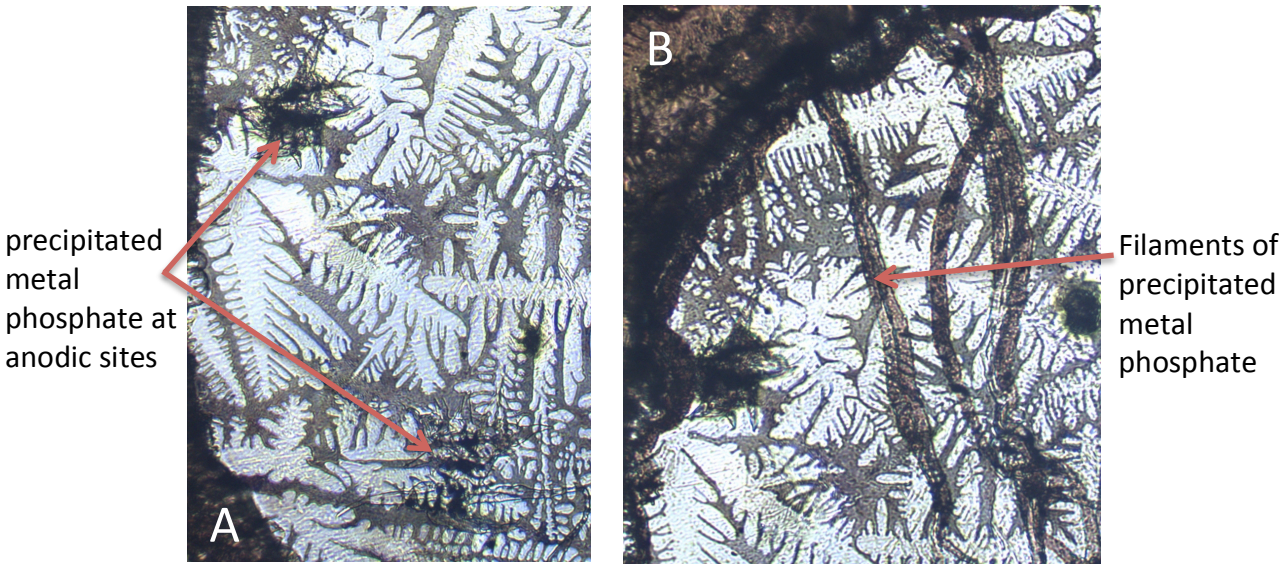

Figure 10. A – A region of ZMA 2 microstructure taken in situ after 6 hours under immersion conditions in 1% NaCl with 1 x 10^{-2} mol/dm^3 Na_3PO_4 additions showing precipitation at anodic sites. B – An image of filamentous precipitates imaged after 30 hours exposure to the electrolyte as in A.

From figure 10 B it was seen that filaments were often composed of two filaments, one having nucleated on the side of the other and this can be observed happening in the video of the time lapse sequence (video 4). It was also seen that the filaments are constrained in their lateral growth whereas forward growth is extremely rapid. Indeed by examination of the individual time-lapse images growth of over 100 μm was observed in the two minute interval between images. This rapidity of precipitation and the independence of precipitation on surface suggest that nucleation and growth from a locally supersaturated solution is occurring. The SEM/EDX data in figure 11 showed that the filaments were rich in magnesium, phosphorous and oxygen indicating that they maybe precipitates of $Mg_3(PO_4)_2$.

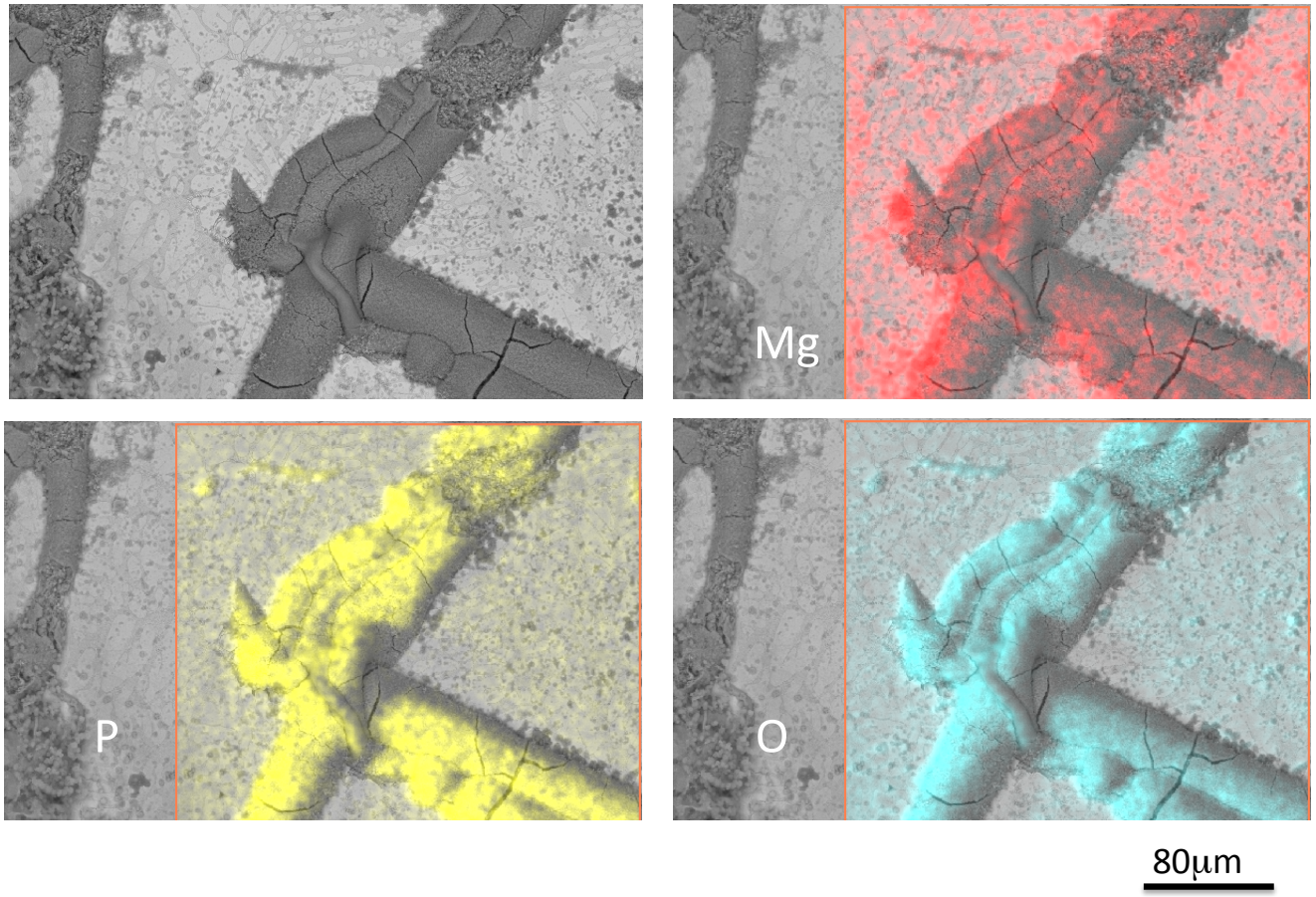

Figure 11. SEM/EDX analysis of a precipitated filament showing it contained Mg, P and O suggesting the deposition of Magnesium Phosphate.

Other EDX data has suggested that some precipitates are composed of zinc phosphate. It is postulated that on exposure to the 1% NaCl solution containing 1 x 10^{-2} mol/dm^3 Na_3PO_4 initial anodic attack occurs on the sample surface releasing metallic ions into solution. As the preferential phase attacked was $MgZn_2$ these ions will be Zn^{2+} and Mg^{2+}. The reaction of these metallic species with phosphate anions (PO_4^{3-}) is required for the production of a precipitate as $Mg_3(PO_4)_2$ and $Zn_3(PO_4)_2$ both have low solubility in water. Local to the anodic sites, metallic ion concentration will be highest with a decreasing concentration profile of ions with distance away from the site. Thus sufficient metallic ions are present to exceed the solubility limit for Zn or Mg phosphates and precipitation is observed local to the anodic sites with a triangular morphology describing the concentration profile away from the anode. The triangular precipitates are quite intriguing. Diffusion of metal ions from a small anodic feature may be expected to give a radial distribution of precipitate as the concentration profile of ions would be expected to follow a Gaussian distribution with distance away from the site. In this case, such a diffusion profile of metal ions may have been established from the anode with the highest levels of supersaturation occurring proximal to the anode thus establishing a preferential site for nucleation and growth of the metal phosphate precipitate. As nucleation and growth of metal phosphate precipitates proceeded local asperities will form at the growing interface. Nucleation of further phosphate precipitates will be more facile on the existing phosphate deposits and diffusion of species to the tip of these features is faster than to the bulk interface and thus growth in the direction of the asperity occurs faster. The width of the feature thus represents a “snapshot” of the local profile of supersaturation out into the solution as established by the diffusion profile.

With continued exposure, further small anodic sites were initiated over the surface of the alloy and thus concentrations of metallic ions continued to build in solution. At these sites rapid precipitation of phosphate occurred and new anodic sites initiated elsewhere on the surface. It would seem that these anodic events generate sufficient metal ions to locally supersaturate the solution that results in precipitation of the phosphate salts onto the surface. It should be stressed that as the solubility of Mg and Zn phosphate are so low, the amount of metal ions entering solution from these anodic events would be of sufficient quantity to exceed the solubility limit of the metal phosphate salts thus allowing the precipitation to occur but significantly less than for the experiment without inhibitor added due to the rapid passivation of the anodic sites. This seems to be supported by the corrosion test data presented in sections 3.4.2 and 3.4.3 where phosphate additions significantly reduce the corrosion rate of the alloy.

The nucleation and rapid filamentous growth subsequently observed suggests that regions of the solution have become supersaturated with metallic ions. Once nucleation occurs, growth then proceeds rapidly due to the ease of further nucleation on the established solid. This would also explain the subsequent formation of new filaments on previously precipitated filaments forming a double width structure as can be seen in figure 10 B. The results indicate that super saturation existed at some distance away from anodic features and indeed on the PTFE tape proximal to the exposed metal. It is intriguing as to why lateral growth of the filaments is so restricted. An explanation could be that growth is pH constrained. Previous research has shown that phosphate inhibition on Mg was dependent on pH levels due to solubility differences between insoluble tertiary phosphate species and soluble primary and secondary phosphates [37]. Lower pH values support the formation of soluble primary and secondary phosphate species and thus this restricted lateral growth maybe as a result of pH differences in solution associated with the formation of anodic and cathodic sites on the metal surface. At present further time-lapse investigations involving altering the concentration of inhibitor, pH of the electrolyte and stirred electrolyte are on going to explore these findings to ascertain whether these postulations are correct.

3.4.2 Polarisation investigations of phosphate on a ZMA alloy

The mechanism of phosphate deposition observed in section 3.4.1 would potentially suggest that phosphate is acting as an anodic inhibitor due to the precipitation proximal to anodic sites in the first instance preventing their growth. Polarisation experiments were performed in order to test this behaviour for samples of ZMA 2 immersed in 1% NaCl pH 7 with no inhibitor, 1% NaCl pH 7 with 1 x 10^{-4} mol/dm^3 Na_3PO_4, and 1% NaCl pH 7 with 1 x 10^{-2} mol/dm^3 Na_3PO_4. The results are shown in figure 12.

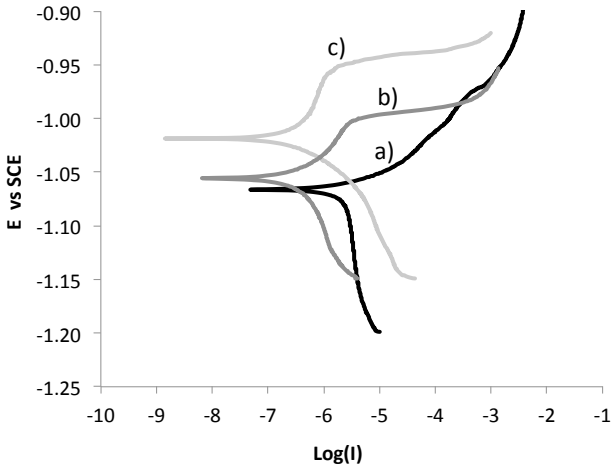

Figure 12. Polarisation results for ZMA 2 immersed in 1% NaCl pH 7 with a) no inhibitor b) 1 x 10^{-4} mol/dm^3 Na_3PO_4 c) 1 x 10^{-2} mol/dm^3 Na_3PO_4

For increasing inhibitor concentrations there was an anodic increase in open circuit potential with a positive shift of 50 mV between the sample with no inhibitor and with 1 x 10^{-2} mol/dm^3 Na_3PO_4 additions. The anodic current also dropped by 2.5 orders of magnitude at a potential of -1V vs SCE for the sample with 1 x 10^{-2} mol/dm^3 Na_3PO_4. As inhibitor concentration was increased a region of passivity was produced with this extending for overpotentials of 40 mV for a phosphate concentration of 1 x 10^{-2} mol/dm^3 Na_3PO_4. These data therefore support the findings of the time-lapse images that indeed phosphate was acting predominantly as an anodic inhibitor in this system.

3.4.3 SVET investigation of phosphate inhibition levels on a ZMA alloy

Samples of ZMA 2 were exposed under immersion conditions to 1% NaCl pH 7 with a) no inhibitor b) 1 x 10^{-4} mol/dm^3 Na_3PO_4 c) 1 x 10^{-2} mol/dm^3 Na_3PO_4. All samples were exposed to the electrolyte for 24 hours with SVET scans of a 100 mm^2 area taken every hour. Once again SVET estimated mass loss was calculated as described in section 2.4.2. The results are shown in figure 13.

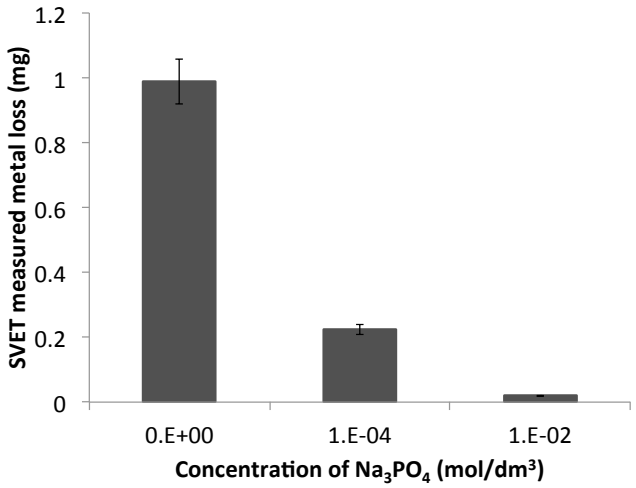

Figure 13. SVET estimated metal loss for the ZMA 2 after 24 hours exposure in 1% NaCl with varying concentrations of Na_3PO_4 inhibitor. A sharp reduction in metal loss was observed for increasing levels of phosphate additions indicating its effectiveness to inhibit corrosion in this alloy.

From figure 13 it was seen that the addition of Na_3PO_4 inhibitor to 1% NaCl had a significant impact on the total corrosion mass loss as measured by SVET. For the 1 x 10^{-4} mol/dm^3 Na_3PO_4 addition a 77% reduction in metal loss was observed with a 98% reduction in metal loss measured for the 1 x 10^{-2} mol/dm^3 Na_3PO_4. These data support the polarisation results in figure 12 that showed a progressive decrease in anodic current for increasing inhibitor additions and the images from time-lapse experiments that demonstrated restricted growth of initiating anodic features.

4. Conclusions

The in situ optical microscopy time-lapse technique has proved extremely valuable for the assessment of preferential phase attack within the microstructures of three ZMA alloy coatings with increasing Mg and Al levels immersed in 1% NaCl pH 7. It was observed that the Mg rich eutectic phases were preferentially corroded in all three ZMA alloys with initial de-alloying of $MgZn_2$ lamellae from the eutectics before wider scale dissolution of Zn rich phases. The progressing fronts of corrosion were always associated with eutectic attack. Image analysis was used to calculate the area of anodic activity for each image in the time-lapse sequences and this was plotted as a function of time. It was observed that the total corroded area decreased as the alloying additions of Mg and Al increased. This may be due to the increased formation of oxides of Mg and Al that have reduced efficiency for cathodic oxygen reduction. SVET 24 hour scans were performed on all three ZMA alloy coatings in 1% NaCl pH 7 and the current density data achieved was integrated and manipulated using Faraday's law to provide an estimated metal loss for each alloy. The same performance trend was observed in the SVET experiments as in time-lapse with increasing alloying additions of Mg and Al decreasing the magnitude of the measured corrosion.

Additions of 1 x 10^{-2} mol/dm^3 Na_3PO_4 to 1% NaCl pH 7 in the time-lapse technique had a dramatic effect on the corrosion observed on ZMA 2. Numerous anodic features nucleated on the sample but were passivated by precipitation of a metal phosphate deposit local to the anodic features. After 15 hours filament like precipitates of phosphate were rapidly deposited on the metal surface with growth of filaments proceeding over the PTFE masking tape. The rapidity of growth and independence of deposition surface suggested a nucleation and growth mechanism from a super saturated solution produced from anodic loss of metal ions in the electrolyte above the corroding metal surface. Polarisation and SVET tests were carried out on ZMA 2 in 1% NaCl pH7 with a) no inhibitor b) 1 x 10^{-4} mol/dm^3 Na_3PO_4 c) 1 x 10^{-2} mol/dm^3 Na_3PO_4. The polarisation tests demonstrated

an anodic shift in potential for increasing inhibitor additions with a drop in current consistent with phosphate behaving as an anodic inhibitor. This seemingly supported the mechanism of action observed in the time-lapse images where precipitation at anodic sites prevented their growth. SVET estimated mass loss showed a dramatic decrease in metal loss as phosphate concentration was increased with a drop of 98% for the 1 x 10^{-2} mol/dm^3 Na_3PO_4 addition compared with the sample with no inhibitor addition.

5. References

[1] F. Goodwin, Galfan Galvanising Alloy Technology, second edition, ILZRO, 1984.

[2] A.R.Marder, Prog. Mater. Sci. 2000, **45**, 191

[3]J. Elvins, J.A. Spittle and D.A. Worsley, Corros. Sci. 2005, **47**, 2740

[4] J. Sullivan, C. Weirman, J. Kennedy, D. Penney, Corros. Sci. 2010, **52**, 1853

[5] D.J.Penney, J.H.Sullivan, D.A.Worsley, Corros. Sci. 2007, **49**, 1321

[6] J Elvins, J.A. Spittle, J.H.Sullivan, D.A.Worsley, Corros. Sci. 2008, **50**, 1650

[7] T. Prosek, A. Nazarov, U. Bexell, D. Thierry, J. Serak, Corros. Sci. 2008, **50**, 2216

[8] T. Prosek, N. Larche, M. Vlot, F. Goodwin, D. Thierry, Mater. Corros. 2010, **61 No 5**, 412

[9] M. Dutta, A. Kumar Halder, S. Brat Singh, Surf. Coat. Tech. 2010,

[10] S. Sugimaru, N. Hikita, A. Yoshie, S. Tanaka, H. Ohba, S. Nishida, Nippon Steel Technical Report, 2007, **96**, 34

[11] S. Schuerz, M. Fleischanderl, G.H. Luckeneder, K. Preis, T. Haunschmied, G. Mori, A.C. Kneissl, Corros. Sci. 2009, **51**, 2355

[12] S. Schürz, G.H. Luckeneder, M. Fleischanderl, P. Mack, H. Gsaller, A.C. Kneissl, G. Mori, Corros. Sci. 2010, **52**, 3271

[13] P. Volovitch, C. Allely, K. Ogle, Corros. Sci. 2009, **51**, 1251

[14] N. Hosking, M. Strom, P Shipway, C Rudd, Corros. Sci. 2007, **49**, 3669

[15] T. Prosek , D. Persson, J. Stoulil, D. Thierry, Corros. Sci. 2014, **86**, 231

[16] N. LeBozec, D. Thierry, M. Rohwerder, D. Persson, G. Luckeneder, L. Luxem, Corros. Sci. 2013, **74**, 379

[17] R. Hausbrand, M. Stratmann, M. Rohwerder, Corros. Sci. 2009, **51**, 2107

[18] M. Vlot, M. Zuijderwijk, M. Toose, L. Elliott, R. Bleeker, T. Maalman in, Proceedings Galvatech 2007, 510

[19] C. Commenda, J. Puhringer, Mater. Charact. 2010, **61**, 943

[20] J. Sullivan, S. Mehraban, and J. Elvins, Corros. Sci. 2011, **53**, 2208

[21] J. Duchoslava, M. Arndta, R. Steinbergera, T. Keppertb, G. Luckenederb, K.H. Stellnbergerb, J. Haglerb, C.K. Rienerb, G. Angelib, D. Stifter, Corros. Sci. 2014, **83**, 327

[22] I.M. Zin, S.B. Lyon , V.I. Pokhmurskii, Corros. Sci. 2003, **45**, 777

[23] A.M. Simões , J. Torres, R. Picciochi, J.C.S. Fernandes, Electrochim. Acta, 2009, **54**, 3857

[24] Kunitsugu Aramaki, Corros. Sci. 2001, **43**, 591

[25] S. M. Powell, H. N. McMurray, D. A. Worsley, Corrosion, 1999, **55**, 1040

[26] D.A. Worsley, D. Williams, J.S.G. Ling, Corros. Sci. 2001, **43**, 2335

[27] F. Thébault, B. Vuillemin, R. Oltra, K. Ogle, C. Allely, Electrochim. Acta, 2008, **53**, 5226

[28] I.M. Zin, S.B. Lyon, A. Hussain, Prog. Org. Coat. 2005, **52**, 126

[29] A.C. Bastos, M.G.S. Ferreira, A.M. Simões, Prog. Org. Coat. 2005, **52**, 339

[30] D. Worsley, H.N. Mcmurray, A. Belghazi, Chem. Comm. 1997, 2369.

[31] S.M. Powell, D.A. Worsley, British Corrosion Journal, 2001, **36**, 42

[32] S. Bohm, H.N. Mcmurray, S.M. Powell, D.A. Worsley, Electrochim. Acta, 2000, **45**, 2165

[33] D.A. Worsley, H.N. McMurray, J.H. Sullivan, I.M. Williams, Corrosion, 2004, **60**, 437

[34] R. Hausbrand, M. Stratmann, M. Rohwerder, Steel Res. Int. 2003, **74**, 453

[35] C. Yao, Z. Wanga, S. L. Tay, T. Zhu, W. Gao, Journal of Alloys and Compounds, 2014, **602**, 101

[36] H. Dafydd, D.A. Worsley, H.N. McMurray, Corros. Sci. 2005, **47**, 3006

[37] G. Williams, H.N. McMurray, R. Grace, Electrochim. Acta, 2010, **55**, 7824